Final Technical Report

Award Number G09AP00074

Investigation into the Nature of Vertical Strong Ground Motion

Martin C. Chapman and Richard W. Godbee

Department of Geosciences
Virginia Polytechnic Institute and State University

4044 Derring Hall, Blacksburg, Virginia, 24061

phone: (540) 231-5036
fax: (540) 231-3386
email: mcc@vt.edu

Project Period: June 1, 2009 - December 31, 2010

Abstract

A full wavefield simulation method was used to investigate geometrical spreading and the relative amplitudes of high-frequency vertical and horizontal components of ground acceleration within 120 km of the source. One-dimensional, horizontally layered velocity models representative of the Appalachian region and the Atlantic coastal plain were used in conjunction with point-source and finite-fault sources. Simulations were done for a grid of receivers with 1-4 km spacing, for a range of focal depths, and for strike-slip and reverse focal mechanisms. The results indicate that apparent geometrical spreading of the geometric mean of randomly oriented horizontal component maximum acceleration amplitudes, averaged over all azimuths, may significantly exceed the ideal theoretical case for far-field body waves in a homogeneous whole space, for hypocentral distances less than approximately 60 km. The behavior of the modeled vertical component is different from the horizontal: vertical component apparent geometrical spreading near the epicenter is much greater, and is strongly dependent on focal mechanism and source depth. The vertical component amplitude versus distance trend flattens in the distance range 60 to 120 km. The rapid decrease of amplitude of the direct S wave on the vertical component leads to a situation where reflections from the mid-lower crust and Moho control the maximum amplitude of the vertical component acceleration in the 60-120 km hypocenter distance range. Near-source vertical component maximum amplitudes averaged over all source-receiver azimuths are almost uniformly less than azimuthally averaged geometric mean horizontal amplitude for the strike-slip focal mechanisms. But near the source of reverse faults, the azimuthally averaged vertical component amplitude equals or exceeds that of the azimuthally averaged mean horizontal. Overall, the modeling indicates that similar vertical and horizontal component geometrical spreading and near-constant horizontal/vertical amplitude ratios observed in connection with the Lg wave at distances mostly greater than approximately 100 km in eastern North America are unlikely to hold at smaller distances. In particular, ground motion prediction models for the vertical component may need to incorporate strong geometrical spreading, and dependence on radiation pattern and focal depth near the source.

Introduction

The amplitude of seismic waves radiated from an isotropic point-source in a homogenous elastic whole space, at source-receiver distance r, is inversely proportional to r in the far-field. However, the velocity structure of the Earth is not homogenous, the earthquake radiation pattern is not isotropic, the source is finite in spatial extent, and the seismic wavefield is usually experienced on an irregular free surface. Consequently, the amplitude-distance function is complicated. It depends on details of the 3-dimensional velocity structure, the source radiation pattern and depth. It also depends on frequency, due to the nature of the earthquake source spectrum and to wave propagation effects involving anelastic loss and scattering. Details of the rupture process in both time and space strongly affect the wavefield near the source of a large earthquake. Because of these and other complications, high-frequency ground motions near the source of large shocks are difficult to model theoretically and empirical ground motion prediction models developed from data recorded in seismically active areas remain the mainstay of earthquake engineering.

Lack of data makes empirical development of strong ground motion prediction models problematic in eastern North America. The data consist largely of recordings obtained at distances in excess of 100 km from earthquakes with magnitudes less than 6. Prior to the recent appearance of the Earthscope transportable array, few earthquakes had been recorded in the eastern United States with more than a handful of calibrated 3-component stations at distances less than 100 kilometers.

We refer below to apparent geometrical spreading, G(r), representing the frequency-independent loss of seismic wave amplitude with increasing hypocenter-receiver distance, r. Idealized far-field body wave spreading in a homogenous whole space is given by $G = r^{-1}$ and $G = r^{-0.5}$ represents idealized surface wave spreading for a half-space. Theoretical studies indicate that apparent geometrical spreading in velocity structures other than a homogeneous whole space will generally involve other variables in addition to r. For example, Ou and Herrmann (1990) found that G(r) may depend upon source depth in layered structures. Burger et al. (1987) note the importance of post-critical reflections from mid-lower crustal velocity discontinuities and the Moho in controlling amplitudes in certain distance ranges.

Empirical studies, using data primarily from earthquakes in southeastern Canada and the northeastern United States, report relatively rapid decay of ground motion amplitude with distance for r less than approximately 60 km, with less rapid decay at distances exceeding approximately 120 km, and a zone of no attenuation (or increasing amplitude with distance) in the intervening distance range (Atkinson and Mereu, 1992, Atkinson, 2004**)**. The flattening of apparent attenuation and/or increase in amplitude observed from approximately 60 to 120 km has been attributed to large amplitude post-critical reflections from the mid-lower crust and Moho (Burger et al., 1987, Atkinson, 2004). The *Lg* phase begins to develop at approximately 120 km or somewhat beyond, depending on crustal structure. *Lg* is a crust-guided phase involving the reflection and interference of multi-path shear waves interacting with the free surface and laterally extensive velocity contrasts in the crust and from the Moho. *Lg* travels with a group velocity of approximately 3.5 km/s and is the largest amplitude phase on all three components for a source in the crust at distances exceeding approximately 120 km. It can be treated as the superposition of higher-mode surface waves, exhibiting geometrical spreading approximately as $r^{-0.5}$ (Wang and Herrmann, 1980; Herrmann and Kijko, 1983, Kennett, 1986).

The lack of well-recorded earthquakes in the distance range $r < 100$ km has prevented detailed empirical investigation of G(r) in terms of other variables. To develop empirical prediction models in this distance range, it has been necessary in the past to combine sparse data from earthquakes in different crustal structure, with different focal depths and mechanisms, as well as recordings of vertical and horizontal components. The resulting scatter exhibited by the combination of these diverse data may be due to the effects of other variables in addition to r.

A related issue is the amplitude of the vertical component, relative to the horizontal components, near the source in eastern North America. Shallow crustal velocities in the mid-continent and Appalachian region are relatively high compared to that found in tectonically active areas such as near major faults in California. Strong velocity contrasts exist in areas of eastern North America where Proterozoic to early Mesozoic high-velocity volcanic, sedimentary or crystalline rocks are overlain at shallow depth by alluvium or deposits of poorly consolidated

Cretaceous and Cenozoic sediments, such as in the Atlantic and Gulf coastal plains and Mississippi embayment. Also, reverse faulting is common in eastern North America, whereas the California strong motion data set is dominated by strike-slip events. The relationship between vertical and horizontal component motions near the source in eastern North America may be different from that inferred from western U.S. data.

This study does not examine the behavior of *Lg*, but instead focuses on hypocenter distances less than 120 km where ground motions are the strongest and maximum acceleration amplitudes for rock sites are largely associated with body wave phase arrivals. The objective is to characterize theoretical behavior of G(r), for horizontal and vertical components, due to strike-slip and reverse faulting focal mechanisms and a range of focal depths. The modeling involves full-wavefield ground motion simulations from both point-source and finite-fault models. The one-dimensional velocity models used are representative of those typical of rock conditions in the mid-continent and Appalachian region, and in the Atlantic coastal plain and Mississippi embayment.

Modeling Approach

Wave propagation effects were modeled using the frequency-wavenumber integration method. The computations were done using the program *hpec96*, version 3.3 (Herrmann, 2002). The program computes elemental Green functions that can be combined to create three-component time series for arbitrarily oriented point-sources, double couples and general moment tensors. The Green functions include all direct and scattered body waves and surface waves for a horizontally layered Earth model with anelastic attenuation. The computed wavefield includes near-field and far-field components. The original source code was modified by the authors to include frequency-dependent Q.

The seismic source was modeled using a kinematic approach following with minor modification that described by Zeng et al. (1994). In that approach the source is comprised of a composite set of overlapping circular subfaults. The subfault radii are randomly distributed according to a power-law with fractal dimension D = 2 (Frankel, 1991). We simulated a moment magnitude M = 6.0 rupture of a square fault with length and width 6.49 km. The dimensions were chosen to be consistent with the M=6 rupture of a circular fault with static stress drop of 100 bars. The constant stress drop of the subevents in the composite model is essentially a free parameter. It largely controls the high-frequency level of the source spectrum. It was constrained by adopting the high frequency level of the Brune (1970) model (M=6.0, static stress drop 100 bars) as a target for the simulation. The average amplitude of the high frequency (greater than 10 Hz) level of the simulation source (moment-rate) spectrum matches that of the target using a subevent stress drop of 35 bars. The simulation assumes a rupture velocity of 2.8 km/sec, with rupture initiating at the center of the rupture zone, which with the aspect ratio of a square fault, minimizes directivity effects and other source complexity. Green functions were not computed for each subfault: the number of required Green functions was reduced by gridding the fault area into 0.25 x 0.25 km elements, summing the subevent source functions of the subfaults within a given grid element, and computing Green functions for the grid elements, rather than all subevents.

The main objective of the study was to characterize the nature of G(r), and for this purpose a point-source rather than a finite-fault source was efficient. In regard to G(r), where r is greater than approximately the source dimension, differences between the point-source and finite-fault simulation are minor for the M=6 earthquake simulated here. The point-source model is simply the composite finite-fault source time function applied at a point, the hypocenter.

Velocity Models

Three velocity models were examined (Figure 1). The "rock-1" and "rock-2" models were based on a review of crustal velocity models developed from long-range seismic refraction experiments in eastern North America (Braile, 1989; Braile et al., 1989; Taylor, 1989; Chulick and Mooney, 2002). The models reflect the range of structures reported for the Appalachian region, and adjacent parts of the craton in southeastern Canada. The crustal thickness of the rock-1 model is 36 km, and the velocity-depth profile is a stepwise increase in velocity approximating a linear gradient. The rock-2 crustal thickness is 40 km, and features a sharp mid-crustal velocity discontinuity and a high-velocity lower crust. The "sediment" model represents the structure in the Atlantic coastal plain in the vicinity of Charleston, South Carolina. The upper 0.75 km of the sediment model was derived from a sonic log and suspension logs described by Chapman et al., (2006). Detailed P and S wave velocities at shallow depths for the rock models are lacking. The uppermost 1 km of both rock models were based on reported S wave velocities of approximately 2.6 - 3.0 km/sec near the surface from a number of shallow geotechnical results in the eastern U.S. and results of Beresnev and Atkinson (1997) for southeastern Canada. The shallow (0 to 0.75 km depth) P and S wave velocities for the rock-1 and rock-2 models were developed by assuming that Poisson's ratio is 0.25 and adjusting the sediment model S wave velocity profile such as to produce 3.0 km/sec velocity at the surface. Adopting this profile for the upper 0.75 km of the rock-1 and rock-2 models was judgmental: the objective was to model, at least to some degree, the decrease in velocity due to effects of near-surface open cracks and weathering. Anelastic attenuation for both rock models and the sub-sediment (deeper than 0.75 km) part of the "sediment" model was modeled using $Q(f) = 811f^{0.42}$ (Chapman and Rogers, 1989), for both P and S waves. A frequency independent Q of 80 was used for P and S waves in all layers at depths less than 0.75 km in the sediment model (Chapman et al., 2008).

Source-Receiver Locations

Figure 2 shows the two receiver patterns used. The finite-fault simulations were done using a square Cartesian grid of stations with receiver spacing of 1 km near the source, 2 km for intermediate distances, (receiver x and y coordinates between +/- 30km and +/- 60 km), and 4 km at larger distances. The point-source simulations were constructed for a pattern of receiver locations arranged as the spokes of a wheel with 5 degree separation: the radial receiver separation was 1 km.

Two focal mechanisms were modeled: right-lateral, strike-slip, on a vertical fault and reverse motion on a fault dipping 45 degrees. The point of rupture initiation (hypocenter) for the finite-fault and the point-source was modeled at depths of 7.25, 12.25, 17.25 and 22.25 km.

Modeling Results

The simulated 3-component ground accelerations were filtered using causal, 4-pole Butterworth bandpass filters in the following frequency bands: 0.5-1.0 Hz, 1.0-2.0 Hz, 2.0-4.0 Hz, 4.0-8.0 Hz, 8.0-16.0 Hz and 16.0-32.0 Hz. The strike-normal and strike-parallel horizontal components were re-oriented by choosing, for each receiver, a random, uniformly-distributed, rotation angle in the range 0 - 360 degrees. The geometric mean of the two maximum (absolute value) horizontal amplitudes was then calculated, for each filter passband: that quantity is referred to below as the "gmran horizontal" amplitude.

Figure 3 shows an example of the finite-fault simulation results in map view, for a focal depth of 12.25 km, and for both strike-slip and reverse mechanisms. The rock-1 velocity model was used for this example. The contours show maximum acceleration values in the 4-8 Hz passband. Figure 4 plots acceleration versus nearest fault-rupture distance for the simulation example shown in Figure 3. The dispersion of the simulated maximum acceleration values at a given nearest fault-rupture distance is largest for the vertical component in the strike-slip simulation. This is largely an effect of the radiation pattern, and interestingly, the dispersion of the vertical component in the reverse fault simulation is less than for the geometric mean of the horizontal components for either of the two focal mechanisms. Figure 4 shows a marked difference in apparent geometrical spreading of the vertical component compared to the horizontal, and a substantial difference of the vertical component amplitudes for the two focal mechanisms. We further examine this behavior and its dependence on frequency, focal depth and velocity structure in the following.

Figures 5 and 6 show plots of the unfiltered acceleration time series for the vertical and strike-normal horizontal components along a profile trending 22 degrees from the strike direction (x direction in Figures 2 and 3). Figure 5 is for the strike-slip fault simulation and Figure 6 shows results for the reverse fault simulation. Rapid attenuation of the direct S wave on the vertical component in the hypocenter distance range from 20 to 60 km, compared to the strike-normal component, is apparent by comparing amplitudes that have been multiplied by the hypocenter distance r, to "correct" for idealized G(r). The direct S wave amplitudes of the horizontal strike-normal component for both mechanisms decay with distance somewhat faster than r^{-1}, whereas the vertical component decays much faster. In the distance range 80 to 120 km, the amplitude of the direct S wave on the vertical component is less than that of the SmS reflection from the Moho (shown by arrows in Figures 5 and 6). On the other hand, the direct S amplitude on the strike-normal horizontal component exceeds the Moho reflection amplitude in this distance range, although the amplitudes are similar, and both phases begin to merge at approximately 120 km.

Figure 7 again shows results in the 4-8 Hz passband, comparing results for the rock-1 and sediment velocity models using a point-source simulation. Plotted are the mean values of maximum acceleration on the vertical and gmran horizontal components, in 2 km-wide distance bins, as a function of hypocenter distance. The lines in Figure 7 are analogous to the short - dashed lines in Figure 4. Results for different focal depths are shown, for both the reverse and strike-slip mechanisms. The sediment model amplifies the 4-8 Hz ground motion relative to the rock-1 model by a factor of approximately 2.5. Figure 7 also shows that the vertical component peak motions exhibit very different apparent geometrical spreading compared to the gmran horizontal components. At hypocenter distances r less than 60 km, the apparent attenuation of the

vertical component with distance is much greater than the horizontals. However, between 60 and 120 km, the amplitude-distance plot for the vertical component flattens, and vertical amplitudes increase at certain distances in this 60-120 km range. The gmran horizontal component amplitudes appear to decay more consistently throughout the distance range examined here, at a rate somewhat greater than r^{-1}. We note also that vertical component amplitudes, relative to the gmran horizontal amplitudes, are larger for the reverse focal mechanism compared to the strike-slip mechanism, and the vertical amplitudes substantially exceed the gmran horizontal amplitude near the epicenter for the rock-1 velocity model and the reverse focal mechanism. Finally, we note that the above-mentioned effects are consistently observed at all focal depths examined.

Figures 8 and 9 extend the comparisons made in Figure 7 to different frequency bands, and compare the two rock velocity models, using a point-source simulation. Figure 8 deals with the strike-slip focal mechanism, and Figure 9 shows results for the reverse faulting mechanism. Figures 8 and 9 show that the behavior of maximum acceleration amplitude for vertical and gmran horizontal component described above for the 4-8 Hz passband persists for the 1-2 Hz and 16-32 Hz passbands.

Figure 10 plots estimates of the slope of the logarithm of maximum amplitude versus log r for the 3 velocity models and 4 different focal depths, in the 6 different filter passbands. These estimates were derived from linear regression of the logarithms of acceleration amplitude on hypocenter distance, in the distance range from 1.5h to 60 km, where h is focal depth. This hypocenter distance range represents the approximately linear section of the log acceleration versus log hypocenter distance plots for the vertical and horizontal components in Figures 8 and 9.

The mean value and standard deviation of all the estimates for the slope of the gmran horizontal component shown in Figure 10 is -1.49 +/- 0.31. It appears that focal depth is not a significant variable in regard to G(r) in the distance range from 1.5h to 60 km, for the gmran horizontal component, and no systematic dependence on frequency is apparent in Figure 10. However, the estimates of slope for the gmran horizontal component for the reverse focal mechanism are systematically steeper (more negative) than for the strike-slip mechanism, for each of the three velocity models examined and for both vertical and gmran horizontal motion.

The range of values of the slope of log maximum amplitude versus log r for the vertical component greatly exceeds that for the gmran horizontal component, and the slope is much steeper. The mean value and standard deviation of all the estimates of slope for the vertical component shown in Figure 10 is -2.63 +/- 0.61. The larger standard deviation for the vertical component reflects the fact that, unlike the gmran horizontal component, the slope for the vertical depends on the focal depth, becoming more negative with increasing depth. The steepest slopes are for the 22.25 km focal depth simulations using the rock-2 model: in that case the hypocenter is beneath the large mid-crustal velocity discontinuity at 19 km in that model (Figure 1), a situation that appears to strongly affect the vertical component G(r) function.

A comparison of Figures 8 and 9 will reveal a contrasting, systematic behavior of the vertical and horizontal components that is largely independent of frequency, distance and focal depth. Beyond a few kilometers from the epicenter of the point-source, the horizontal component (gmran) amplitudes are smaller for the reverse faulting mechanism, compared to the strike-slip faulting mechanism. In contrast, the vertical component amplitudes are larger for the reverse

faulting mechanism, compared to the strike-slip mechanism. Figure 11 plots the ratio of the mean acceleration for the reverse focal mechanism to that for the strike-slip focal mechanism, as a function of hypocenter distance, in 2 km-wide distance bins, for the rock-1 and soil velocity models. The vertical component is systematical larger for the reverse focal mechanism compared to the strike-slip focal mechanism, over most of the hypocenter distance range, whereas the geometric mean of the randomly oriented horizontal components (gmran) is systematically smaller for the reverse mechanism, compared to the strike-slip focal mechanism, at epicenter distances beyond a few kilometers. This is the case regardless of focal depth, frequency band or velocity model and is therefore due to the source radiation pattern.

Conclusions

Full wavefield simulations using layered, 1-D velocity structures shows that apparent geometrical spreading of the geometric mean of the maximum acceleration amplitudes of two randomly oriented, orthogonal, horizontal components (gmran), averaged over all azimuths from the source, significantly exceeds the ideal case for body waves in a homogeneous whole space, for hypocentral distances less than approximately 60 km. These observations are based on the mean values of bandpass-filtered maximum acceleration amplitudes, binned according to hypocenter distance, using a very large number of receiver locations surrounding the source.

The behavior of the maximum amplitude and the apparent geometrical spreading of the vertical component ground acceleration differ from that of the geometric mean of the randomly oriented horizontal component, at frequencies greater than 0.5 Hz examined here. At hypocenter distances r in the range $1.5h < r < 60$ km, where h is focal depth, the apparent geometrical spreading of the vertical component G(r) of the vertical greatly exceeds that of the gmran horizontal, and ranges approximately from $r^{-1.5}$ to $r^{-4.0}$. This wide range for the vertical component apparent geometrical spreading at small distance from the epicenter is because of strong dependence on both focal depth and focal mechanism. Apparent geometrical spreading of the vertical component at distances less than 60 km is more rapid for greater focal depths, and is systematically more rapid for reverse focal mechanisms (compared to strike-slip) at all depths modeled. Beyond 60 km, the modeled direct S wave on the vertical component (averaged over all source-receiver azimuths) is smaller than the vertical component amplitude of reflections from the mid-crust and Moho, resulting in a zone extending from 60 km to the 120 km limit of the modeling in which maximum amplitudes on the vertical component (averaged over 360 degrees of azimuth from source) do not decay with distance. This behavior occurred for all three velocity structures examined here, and was independent of frequency.

In contrast to results for the vertical component, the geometric mean of the maximum amplitudes of two randomly oriented, orthogonal horizontal components (gmran) at distances in the range $1.5h<r<60$ km for rock sites displays geometrical spreading as approximately $r^{-1.3}$ for strike-slip and $r^{-1.5}$ for reverse faulting mechanisms, with no significant dependence on focal depth. The apparent geometrical spreading for the deep sediment model is somewhat greater than for the rock models: roughly $r^{-1.5}$ for strike-slip and $r^{-1.9}$ for reverse faulting mechanisms. The geometric mean of the randomly oriented horizontal maximum amplitudes of the direct S wave (averaged over 360 degrees of azimuth) in all the velocity models equals or exceeds that of the Moho and/or lower crustal reflections throughout the distance range examined (to 120 km) and the gmran horizontal component amplitudes do not exhibit the marked flattening of the vertical component G(r) function in the 60 to 120 km distance range.

The amplitudes of the vertical and geometric mean amplitudes of the randomly oriented horizontal components show additional contrasting behavior. Vertical component amplitudes are from 1 to 2.5 times greater for reverse faulting focal mechanisms, compared to the vertical component amplitudes from the strike-slip focal mechanisms in the hypocenter distance range from approximately 1.5 times the focal depth to the limit of the modeling at 120 km. The geometric mean amplitudes of the randomly oriented horizontal components in the same distance range show opposite behavior: the strike-slip mechanisms result, on average, in larger horizontal component motions, relative to reverse, by factors ranging from 1 to 1.7. These observations are largely independent of focal depth and frequency.

The modeling exercise suggests that near-source ground motion predication models must treat the vertical and horizontal component motions separately because they exhibit different behavior in terms of amplitude as a function of distance, as well as dependence on focal mechanism and focal depth. Assumptions concerning the ratios of horizontal to vertical component amplitudes that are based on observed behavior of the different components at distances greater than approximately 100 km may not hold at smaller distances, where the modeled amplitude-distance relationship for the vertical component is different from that of the geometric mean of the two horizontal component amplitudes. Further, accurate prediction of the vertical component amplitudes in this distance range may require more complicated prediction models than those for the horizontal components, because the modeled vertical amplitudes are more strongly dependent on focal mechanism radiation pattern and focal depth. Finally, the modeling suggests that vertical component amplitudes near the epicenters of reverse faulting earthquakes can be expected to significantly exceed that of the gmran horizontal components, when the observations are averaged over a sufficiently wide range of azimuths.

References

Atkinson, G.M. (2004). Empirical attenuation of ground-motion spectral amplitudes in southeastern Canada and the northeastern United States, *Bull. Seism. Soc. Am.* **94,** 1079-1095.

Atkinson, G. and R. Mereu (1992). The shape of ground motion attenuation curves in southeastern Canada, *Bull. Seism. Soc. Am.* **82,** 2014-2031.

Beresnev, I.A. and G.M. Atkinson (1997). Shear-wave velocity survey of seismographic sites in eastern Canada: calibration of empirical regression method of estimating site response, *Seismol. Res. Lett.* **68,** 981-987.

Braile, L.W. (1989). Crustal structure of the continental interior, in *Geophysical Framework of the Continental United States* L.C. Pakiser and W.D. Mooney (Editors), Memoir 172, Geological Society of America, Boulder, Colorado, 285-315.

Braile, L.W., Hinze, W.J., von Frese, R.R.B., and G.R. Keller (1989). Seismic properties of the crust and uppermost mantle of the conterminous United States and adjacent Canada, in *Geophysical Framework of the Continental United States* L.C. Pakiser and W.D. Mooney (Editors), Memoir 172, Geological Society of America, Boulder, Colorado, 655-680.

Brune, J.N. (1970). Tectonic stress and the spectra of seismic shear waves from earthquakes, *J. Geophys. Res.* **75,** 4997-5009.

Burger, R.W., P.G. Somerville, J.S. Barker, R.B. Herrmann and D.V. Helmberger (1987). The effect of crustal structure on strong ground motion attenuation relations in eastern North America, *Bull. Seism. Soc. Am.* 77, 420-439.

Chapman, M.C., J.N. Beale and R.D. Catchings (2008). Q for P-waves in the sediments of the Virginia Coastal Plain, *Bull. Seism. Soc. Am.* **98,** 2022-2032.

Chapman, M.C., J.R. Martin, C.G. Olgun, and J.N. Beale (2006). Site-Response models for Charleston, South Carolina, and vicinity developed from shallow geotechnical investigations, *Bull. Seism. Soc. Am.* **96,** 467-489.

Chapman, M.C. and M.J.B. Rogers (1989). Coda Q in the Southern Appalachians, *Geophys. Res. Lett.* **16**, 531-534.

Chulick, G.S. and W. D. Mooney (2002). Seismic structure of the Crust and uppermost Mantle of North America and Adjacent Ocean Basins: A synthesis, *Bull. Seism. Soc. Am*. 92, 2478-2492.

Frankel, A. (1991). High-frequency spectral falloff of earthquakes, fractal dimension of complex rupture, b-value, and the scaling of strength on faults, *J. Geophys. Res.* **96**, 6291-6302.

Haskell, N. A. (1953). Dispersion of surface waves in multilayered media, *Bull. Seism. Soc. Am.* **43**, 17-34.

Haskell, N. A. (1962). Crustal reflection of plane P and SV waves, *J. Geophys. Res.* **67**, 4751-4767.

Herrmann, R.B. (2002). An Overview to Synthetic Seismogram Computation, in software distribution *Computer Programs for Seismology*, St. Louis University, St. Louis, Missouri, http://www.eas.slu.edu/People/RBHerrmann/CPS330.html, (last accessed August 19, 2010), 183 p.

Herrmann, R.B. and A. Kijko (1983). Modeling some empirical vertical component *Lg* relations, *Bull. Seism. Soc. Am.* **73**, 157-171.

Herrmann, R.B. (1975). A student's guide to the use of P and S wave data for focal mechanism determination, *Earthquake Notes*, **46**, 29-40.

Kanamori, H. and D.L. Anderson (1975). Theoretical basis for some empirical relations in seismology, *Bull. Seism. Soc. Am*. **65**, 1073-1095.

Kennett, B.L.N. (1986). *Lg* waves and structural boundaries, *Bull. Seism. Soc. Am.* **76**, 1133-1141.

Ou, G.-B. and R.B. Herrmann (1990). A statistical model for ground motion produced by earthquakes at local and regional distances, *Bull. Seism. Soc. Am.* **80**, 1397-1417.

Silva, W. (1976). Body waves in a layered anelastic solid, *Bull. Seism. Soc. Am,* **66**, 1539-1554.

Taylor, S.R., (1989). Geophysical framework of the Appalachians and adjacent Grenville Province, in *Geophysical Framework of the Continental United States* L.C. Pakiser and W.D. Mooney (Editors), Memoir 172, Geological Society of America, Boulder, Colorado, 317-348.

Wang, C.Y. and R.B. Herrmann (1980). A numerical study of P-, SV-, and SH- wave generation in a plane layered medium, *Bull. Seism. Soc. Am.* **70**, 1015-1036.

Zeng, Y., J.G. Anderson and G. Yu (1994). A composite source model for computing realistic synthetic strong ground motions, *Geophys. Res. Lett.* 21, 725-728.

Figures

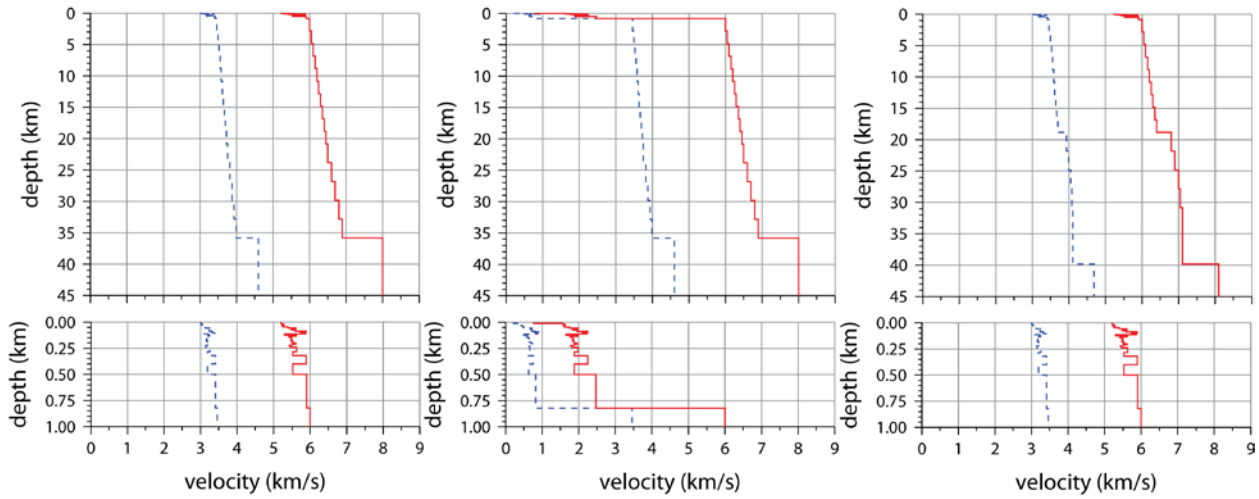

Figure 1. *Left:* "rock-1" velocity model. Center: "sediment" model. *Right:* "rock-2" model. The dashed line shows S wave velocity, the solid line shows P wave velocity.

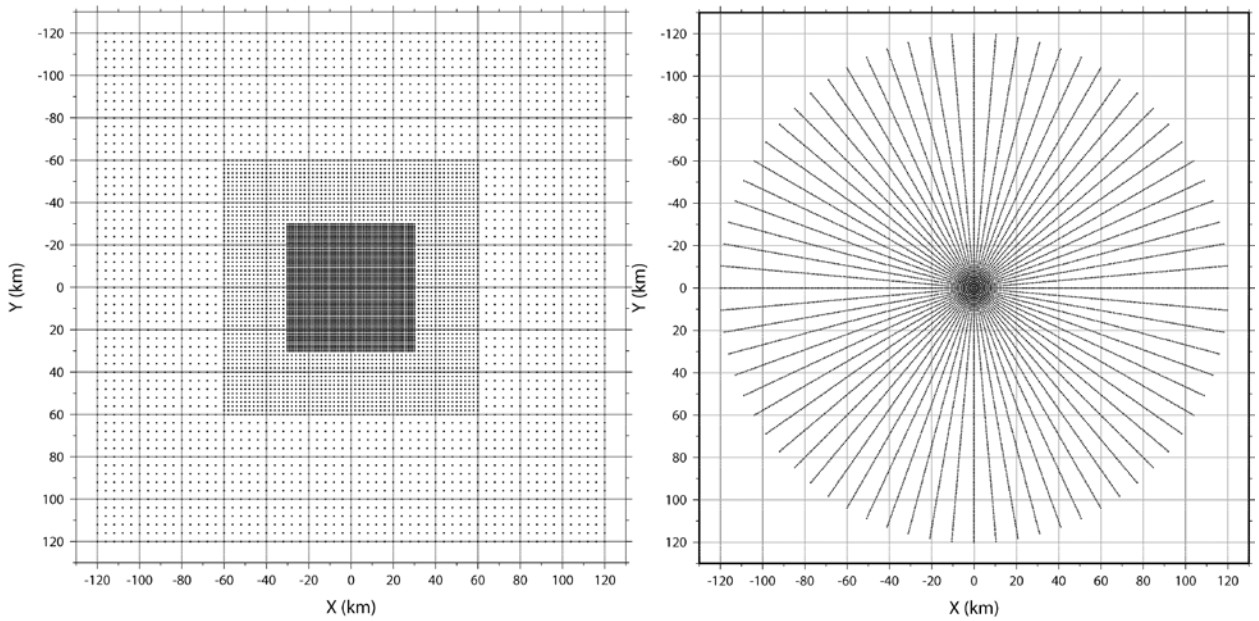

Figure 2. *Left:* Cartesian grid used for finite-fault simulation. *Right:* Polar grid used for point-source simulation.

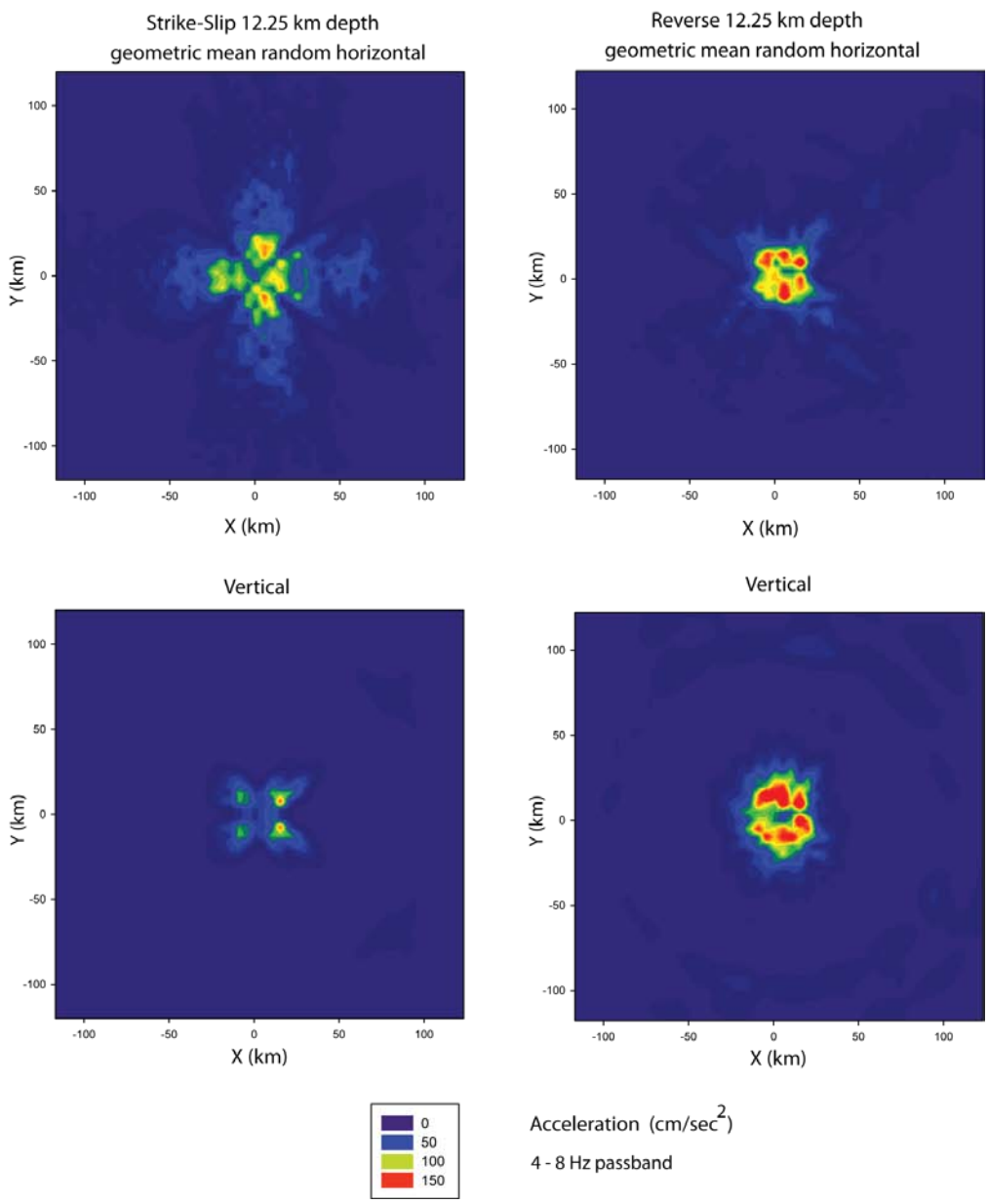

Figure 3. Simulated maximum acceleration amplitudes in the 4-8 Hz band for a M 6.0 event with center of rupture at 12.25 km depth, striking in the x direction. The rock-1 velocity model was used for the finite-fault simulation. *Upper left and lower left:* Geometric mean of the maximum amplitudes of two orthogonal randomly orientated horizontal components, and the vertical component, respectively, for a right-lateral strike-slip focal mechanism. *Upper right, lower right:* Geometric mean of the maximum amplitudes of two orthogonal randomly orientated horizontal components, and the vertical component, respectively, reverse faulting mechanism, with the fault dipping 45 degrees in the negative y direction. The rupture initiation was at the center of a square rupture area, as described in the text.

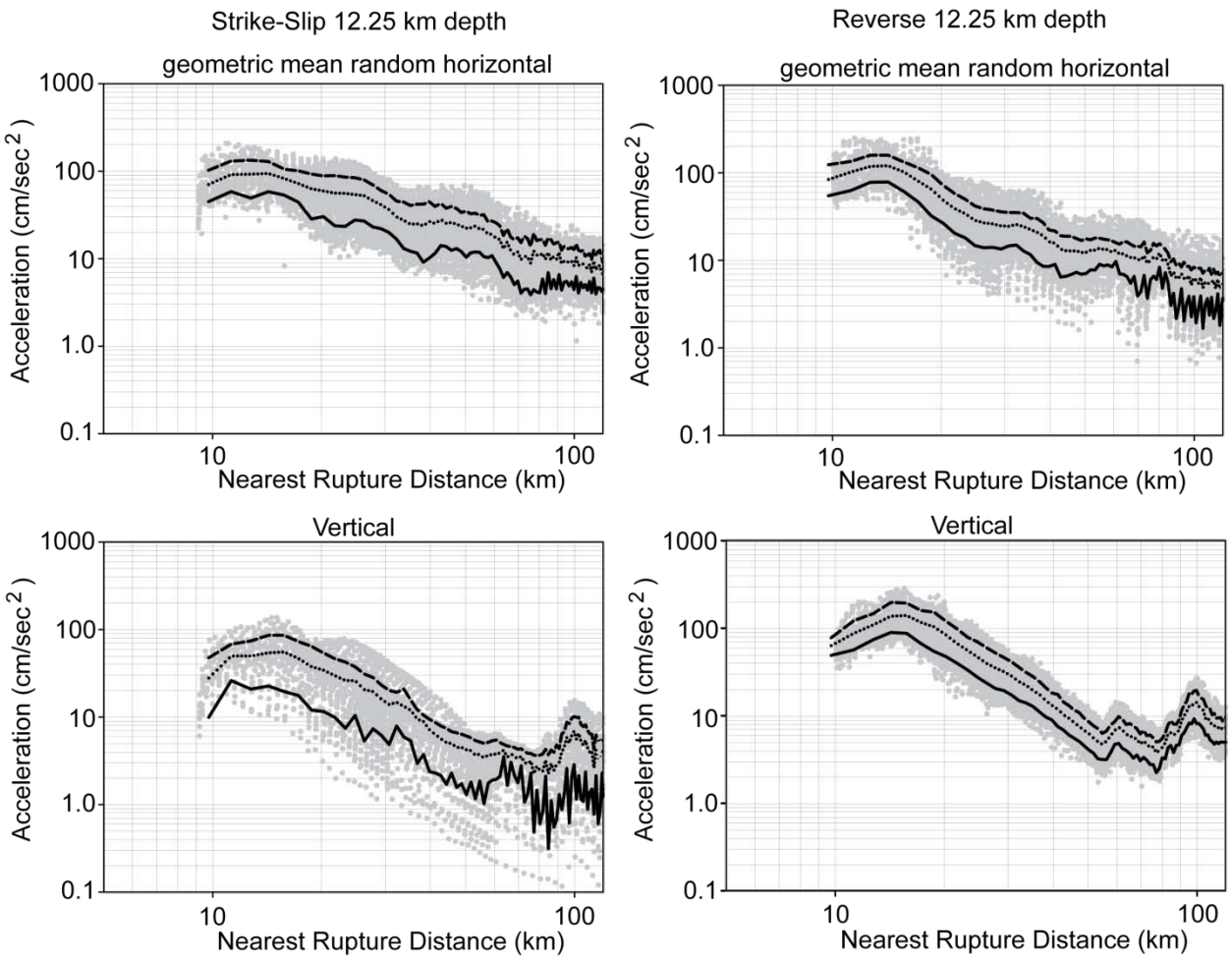

Figure 4. The grey dots show simulated maximum acceleration amplitudes in the 4-8 Hz band plotted versus distance to the nearest point of fault rupture, for a M 6.0 event with center of rupture (hypocenter) at 12.25 km depth, as shown in map view in Figure 3. The rock-1 velocity model was used for the finite-fault simulation. *Upper left and lower left:* The geometric mean of the two randomly orientated orthogonal horizontal components, and the vertical component, respectively, for a strike-slip focal mechanism. *Upper right, lower right:* The geometric mean of the two randomly orientated orthogonal horizontal components, and the vertical component, respectively, reverse faulting mechanism, with the fault dipping 45 degrees. The means of the simulated values in distance bins 2 km wide are shown by the short-dash line: 16th and 84th percentile values are shown by the solid and long-dash lines, respectively.

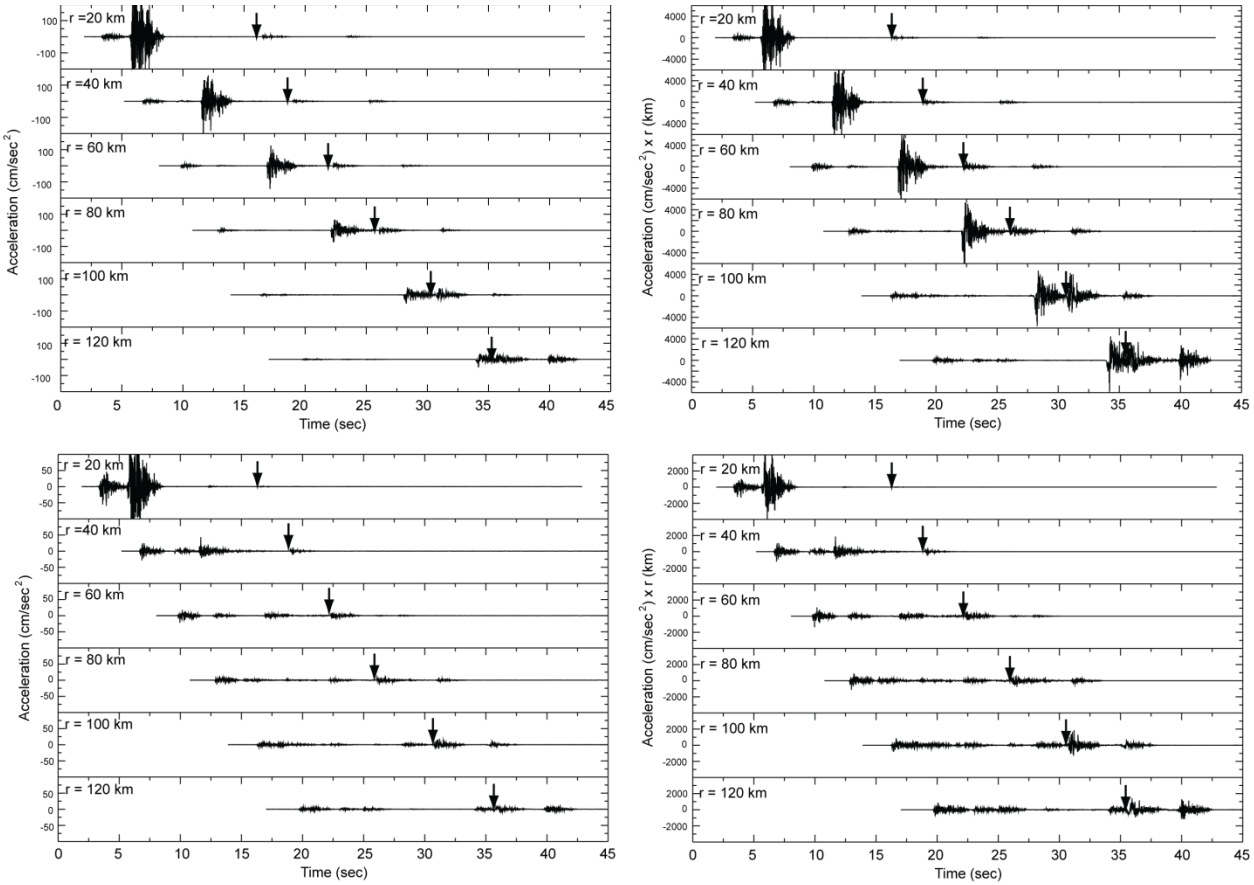

Figure 5. Acceleration waveforms for the finite-fault simulation, M=6.0, strike-slip, hypocenter depth 12.25 km, rock-1 velocity model, along a profile trending 22 degrees from the strike direction. *Upper left*: strike-normal horizontal component. *Upper right*: strike-normal horizontal component multiplied by the hypocenter distance r. *Lower left*: vertical component. *Lower right*: vertical component multiplied by the hypocenter distance r. Arrows indicate SmS reflection from the Moho. Note the very rapid attenuation of the direct S wave on the vertical component, compared to the strike-normal component. At distances exceeding 60 km the vertical component maximum amplitude is associated with the Moho reflection.

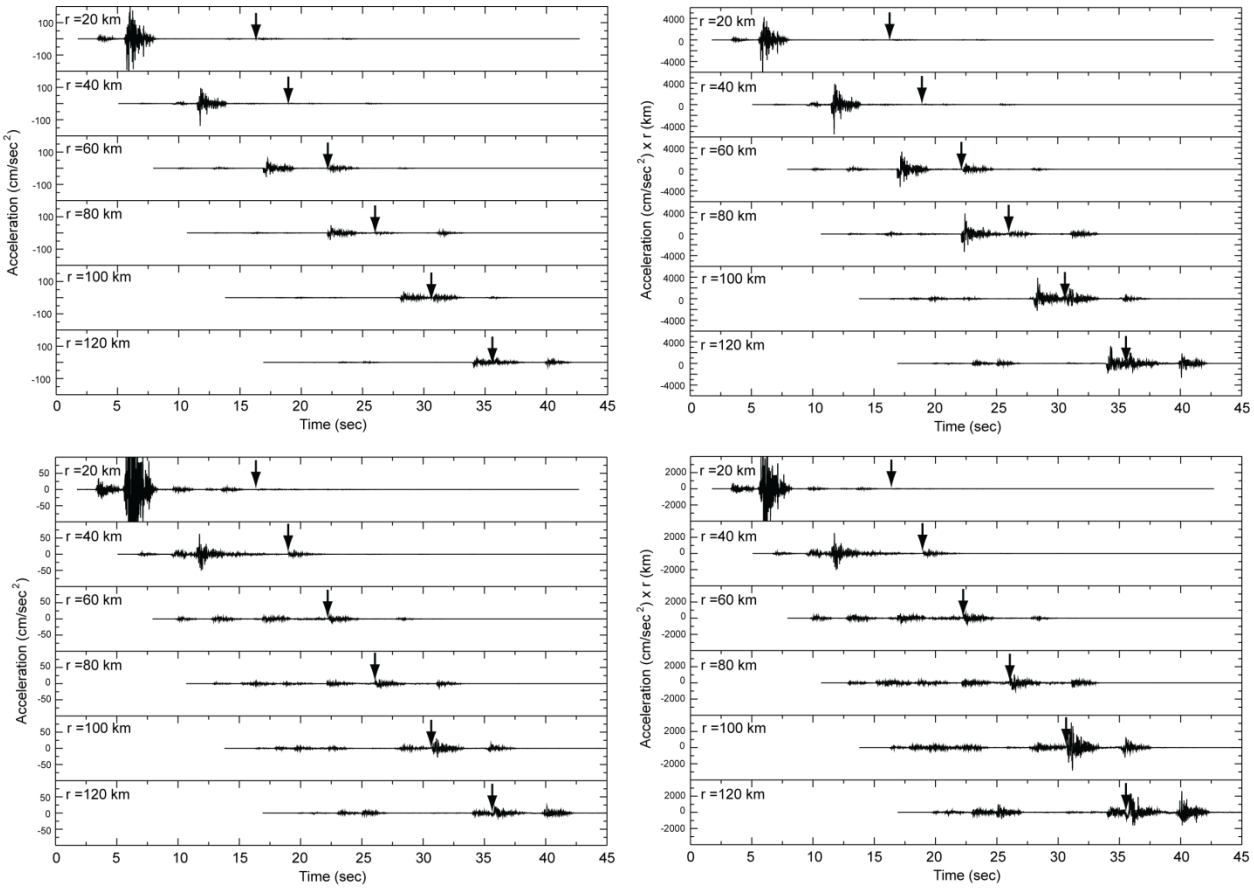

Figure 6. Acceleration waveforms for the finite-fault simulation, M=6.0, reverse fault, hypocenter depth 12.25 km, rock-1 velocity model, along a profile trending 22 degrees from the strike direction. *Upper left*: strike-normal horizontal component. *Upper right*: strike-normal horizontal component multiplied by the hypocenter distance r. *Lower left*: vertical component. *Lower right*: vertical component multiplied by the hypocenter distance r. Arrows indicate SmS reflection from the Moho. Note the very rapid attenuation of the direct S wave on the vertical component, compared to the strike-normal component. At distances exceeding 60 km the vertical component maximum amplitude is associated with the Moho reflection.

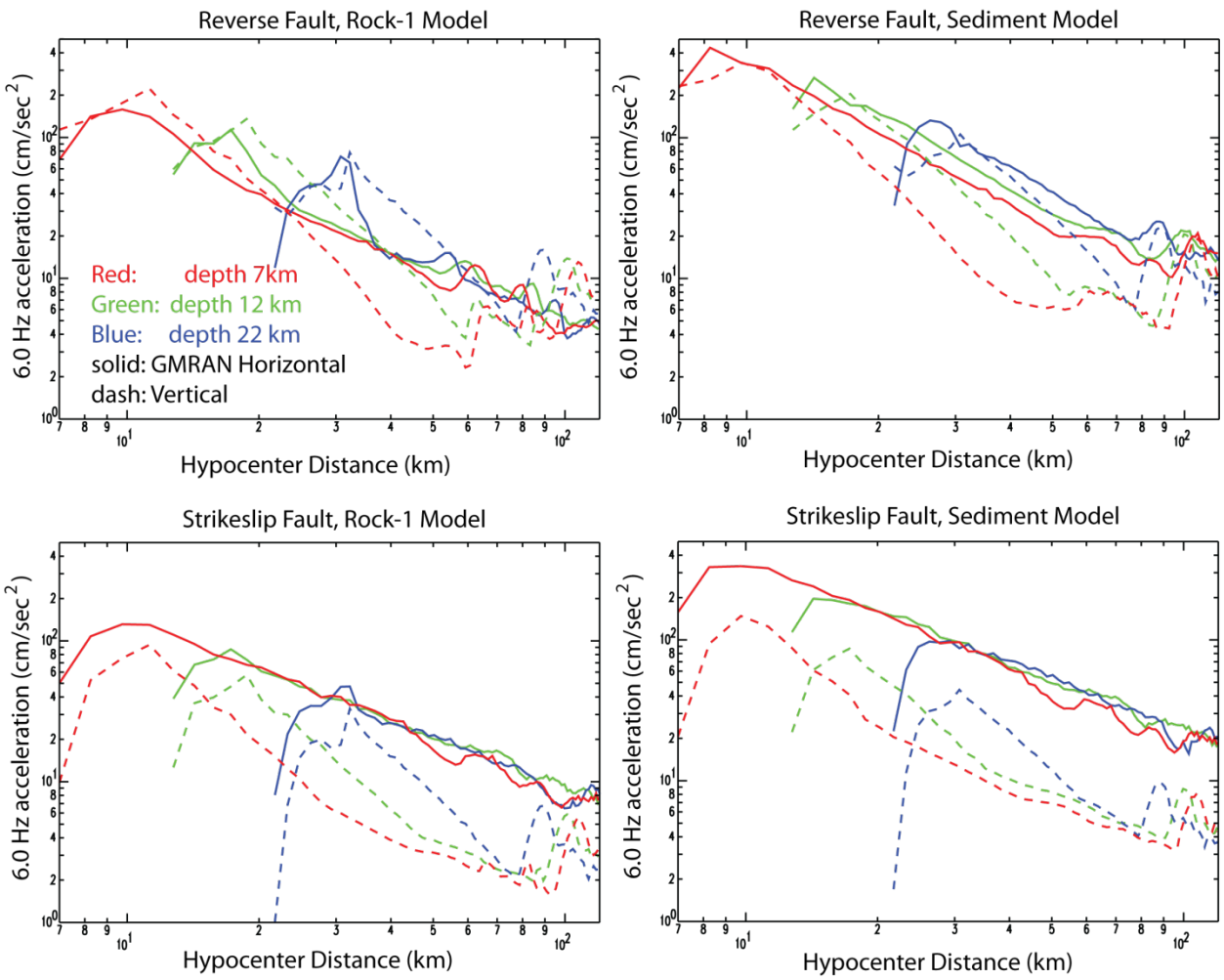

Figure 7. *Upper left and lower left:* mean values for maximum acceleration for the 4-8 Hz frequency band in 2km-wide distance bins, rock-1 velocity model, for three different focal depths, reverse and strike-slip mechanisms, respectively. The solid lines show values for the geometric mean of the two randomly oriented orthogonal horizontal components (GMRAN). The dashed lines show values for the vertical component. *Upper right: and lower right:* corresponding results for the sediment velocity model.

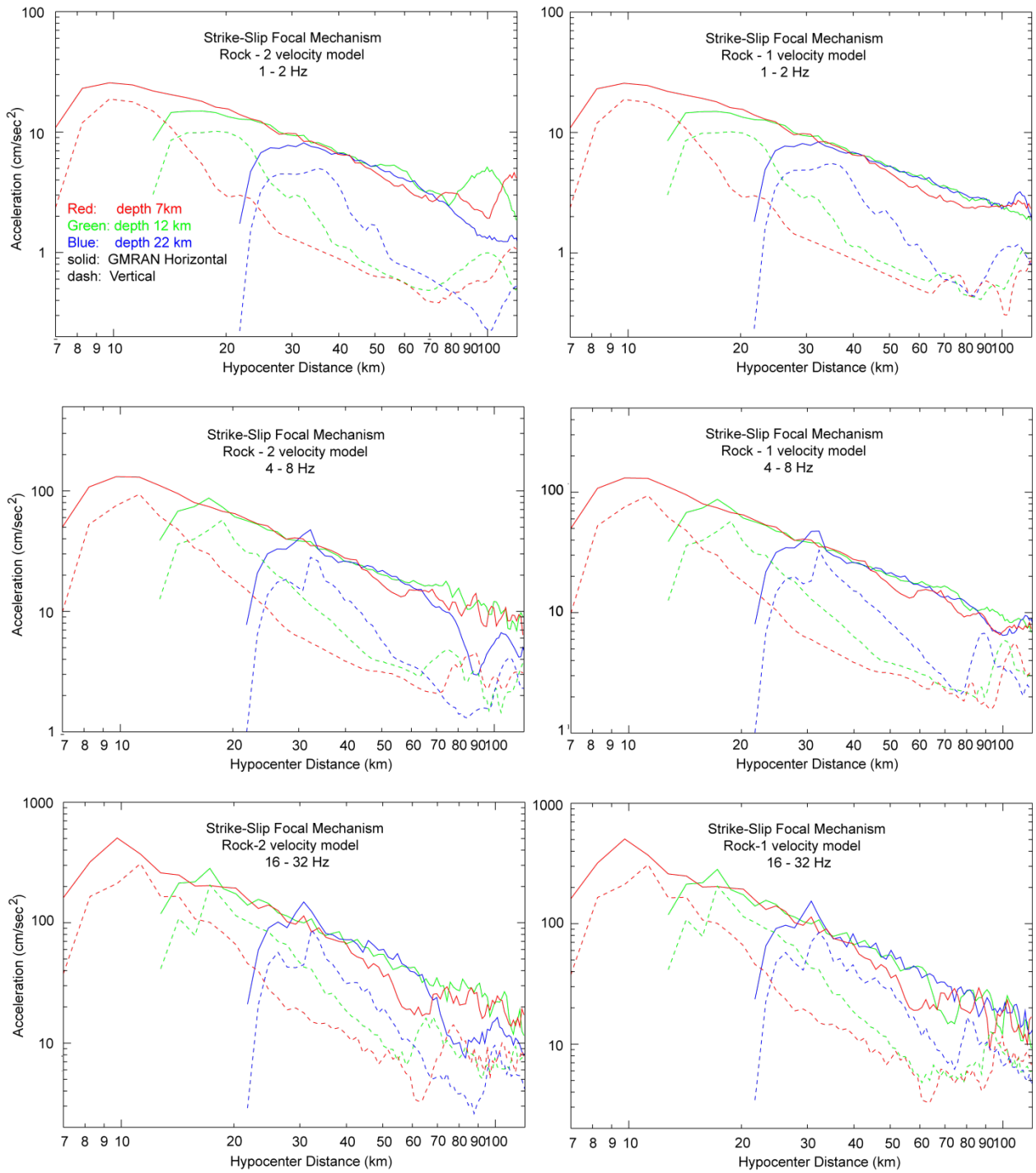

Figure 8. Mean values of maximum acceleration for the 1-2 Hz, 4-8 Hz and 16-32 Hz frequency bands in 2 km-wide distance bins, for the rock-2 *(left column)* and rock-1 *(right column)* velocity models, three different focal depths, and strike-slip mechanism. The solid lines show values for the geometric mean of the two randomly oriented orthogonal horizontal components (GMRAN). The dashed lines show values for the vertical component.

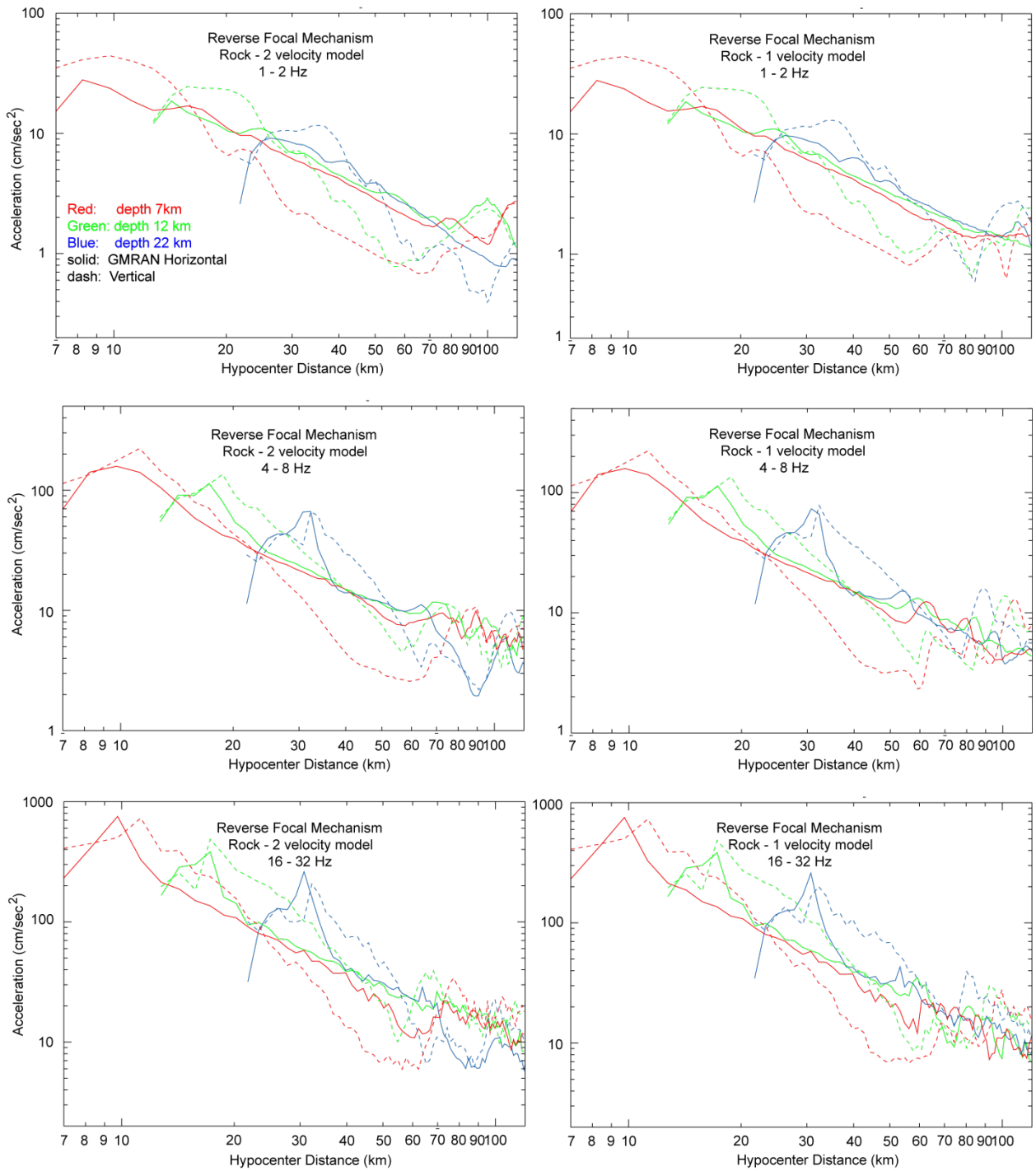

Figure 9. Mean values of maximum acceleration for the 1-2 Hz, 4-8 Hz and 16-32 Hz frequency bands in 2 km-wide distance bins, for the rock-2 *(left column)* and rock-1 *(right column)* velocity models, three different focal depths, and reverse focal mechanism. The solid lines show values for the geometric mean of the two randomly oriented orthogonal horizontal components (GMRAN). The dashed lines show values for the vertical component.

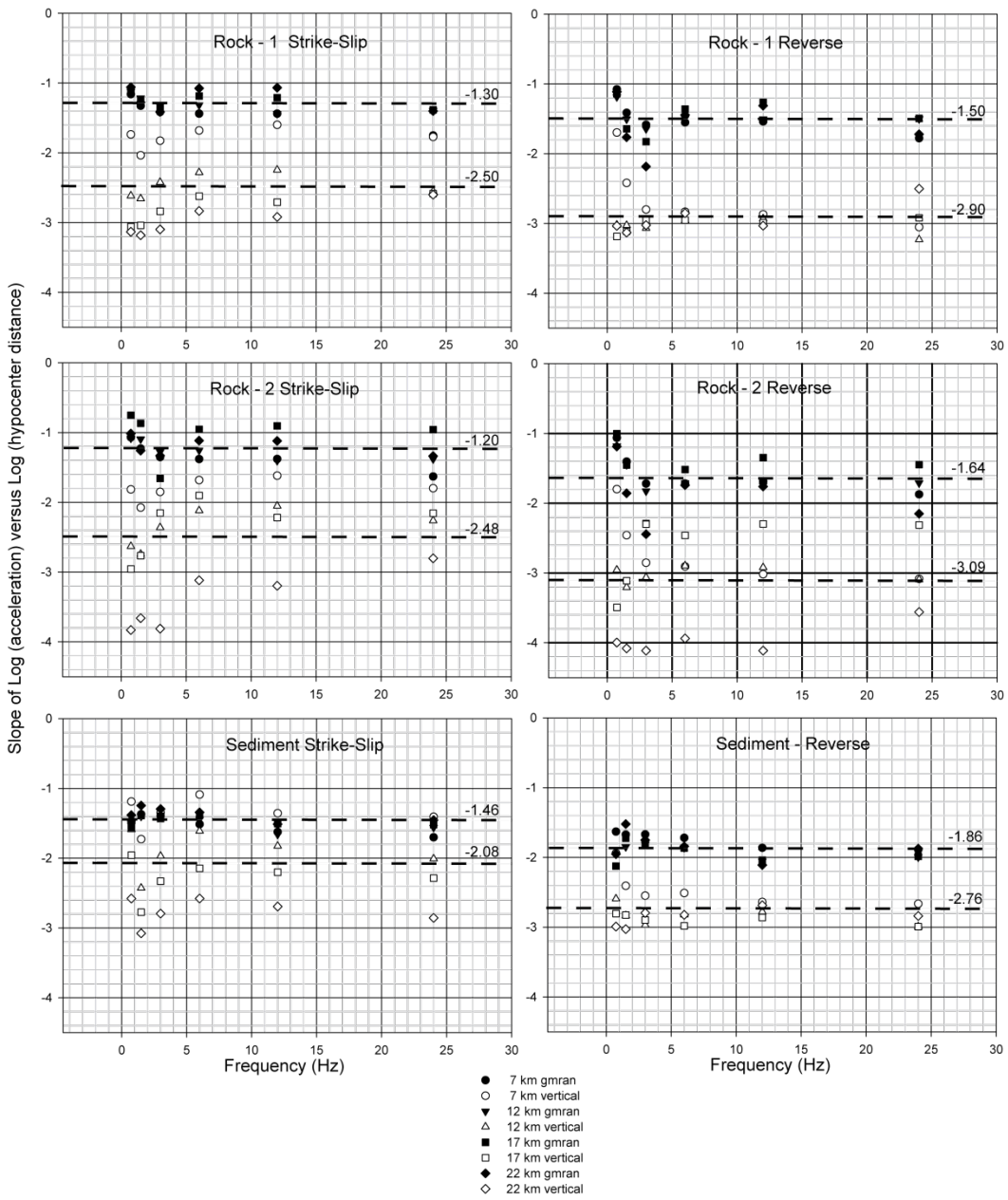

Figure 10. The slope of a linear regression of the logarithm of maximum acceleration on the logarithm of hypocenter distance for each of the rock-1, rock-2 and sediment velocity models, as a function of bandpass filter center frequency, for focal depths of 7.25, 12.25, 17.25 and 22.25 km, vertical and geometric mean of randomly oriented horizontal components (gmran). The values plotted are estimates of η for $G(r) = r^{\eta}$, derived from all simulations in the hypocenter distance ranges 10-60 km, 18-60 km, 25-60 km and 33-60 km for focal depths 7.25 *(circles)*, 12.25 *(triangles)*, 17.25 *(squares)* and 22.25 km *(diamonds)*, respectively. Filled symbols are for the gmran horizontal component, open symbols are for the vertical component. Dashed lines with numbers indicate mean estimates, averaged over focal depth and frequency.

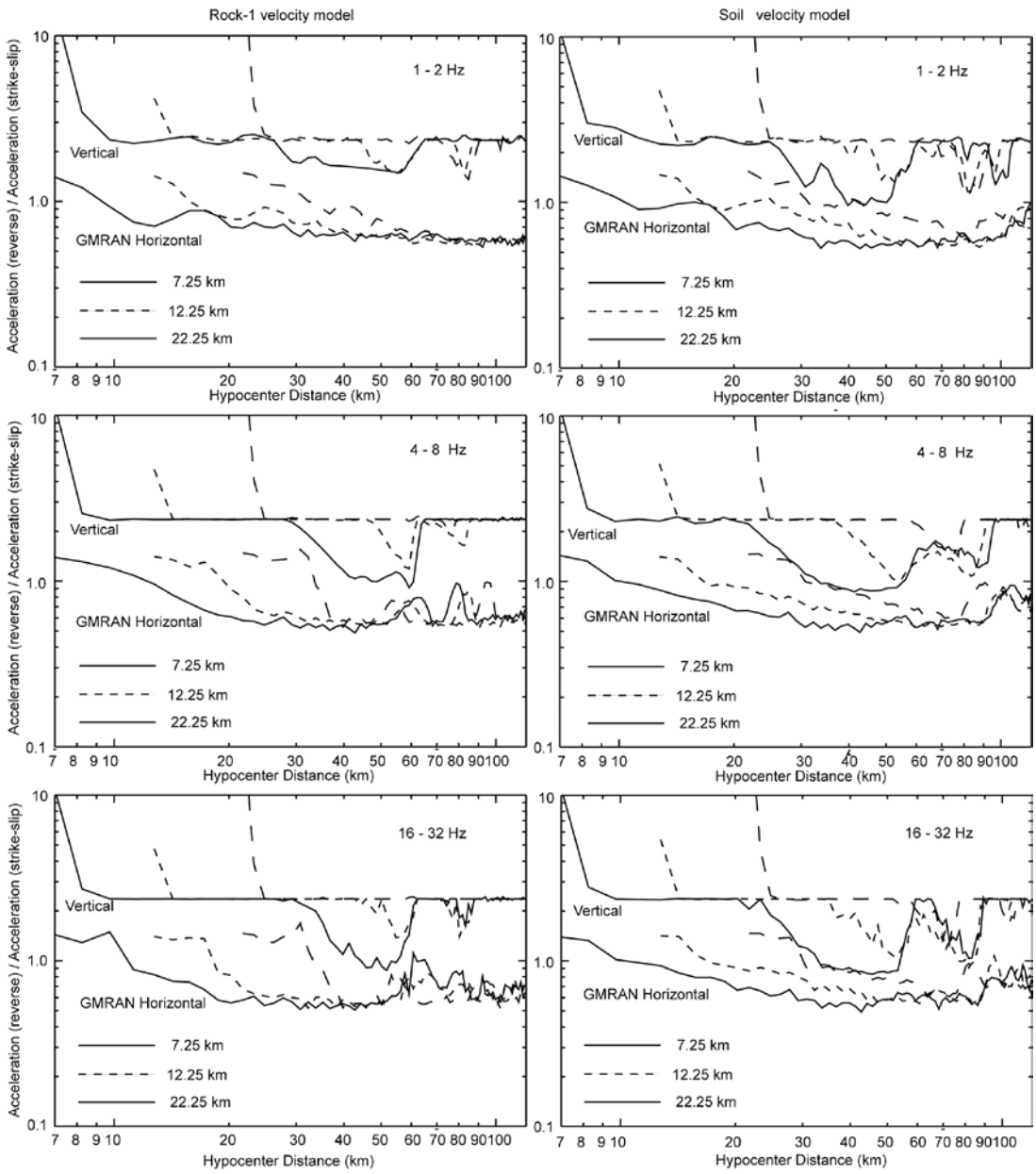

Figure 11. The ratio of the mean acceleration for reverse focal mechanism to that for strike-slip focal mechanism, as a function of hypocenter distance, in 2 km wide distance bins, for the rock-1 velocity model *(left column)* and the sediment velocity model *(right column)*, for point-sources. Shown are results for 3 focal depths, and 3 filter passbands. The vertical component is systematical larger for the reverse focal mechanism compared to the strike-slip focal mechanism, over most of the hypocenter distance range, whereas the geometric mean of the randomly oriented horizontal components (GMRAN) is systematically smaller for the reverse mechanism, compared to the strike-slip focal mechanism, at epicenter distances beyond a few kilometers.